Unusual structure and morphology of cellulose nanocrystals obtained by room temperature acid extraction: effect of cellulose source and pretreatment

Carbohydrate Polymer Technologies and Applications 14 (2026) 101125

Contents lists available at ScienceDirect

Carbohydrate Polymer Technologies and Applications

journal homepage: www.sciencedirect.com/journal/carbohydrate-polymer-technologies-and-applications

Unusual structure and morphology of cellulose nanocrystals obtained by room temperature acid extraction: effect of cellulose source and pretreatment

Andrea Riccioni [a], Jean-Luc Putaux [b], Matthieu Fumagalli [b,c], Silvia Maria Ronchetti [a], Sara Ferraris [a], Roberta Bongiovanni [a], Alessandra Vitale [a,*]

[a] Politecnico di Torino, Department of Applied Science and Technology, 10129 Torino, Italy
[b] Université Grenoble Alpes, CNRS, CERMAV, 38000 Grenoble, France
[c] Université Claude Bernard Lyon 1, INSA Lyon, Université Jean Monnet, CNRS UMR 5223, Ingénierie des Matériaux Polymères, 69622 Villeurbanne, France

ARTICLE INFO

Keywords:
Cellulose nanocrystals (CNCs)
Room-temperature acid hydrolysis
Nanocellulose morphology
Mercerization
Polysaccharide crystallinity

ABSTRACT

Cellulose nanocrystals (CNCs) are attracting increasing interest as renewable nanomaterials for composite fillers and rheological modifiers. Their properties depend on morphology and crystalline structure, governed by cellulose source and hydrolysis conditions. Conventionally, CNCs are extracted by acid hydrolysis at elevated temperatures, favoring rapid depolymerization and limiting alternative reorganization pathways. Herein, sulfuric acid hydrolysis was performed at room temperature as a structure-directing approach to investigate how cellulose source, crystalline polymorphism, and mercerization pretreatment influence CNC formation. Hemp pulp, micronized cellulose powder, and microfibrillated cellulose were studied in native and mercerized forms. Suppressing thermal activation alters the balance between depolymerization, solubilization, and recrystallization, leading to CNCs with distinct crystalline structures and non-classical morphologies. In addition to typical rod-like nanocrystals, hierarchical and flake-like nanoparticles were obtained, including larger particles several hundred nanometers long (average length ≈320 nm) decorated with smaller cellulose II crystallites (≈45 nm length, ≈15 nm width). The results demonstrate that the interplay between cellulose source, pretreatment, and hydrolysis conditions governs CNC morphology and polymorphism. This study provides mechanistic insight into CNC formation under low-temperature acid hydrolysis and demonstrates how controlled access to unconventional CNC architectures and surface features can be exploited for rational design of cellulose-based nanomaterials for advanced applications.

1. Introduction

Thanks to its unique combination of mechanical strength, renewability, and surface chemistry, cellulose provides a versatile platform for designing advanced materials. Cellulose is a linear homopolymer of glucose units linked via β-1,4 glycosidic linkages (Seddiqi et al., 2021). It is considered to be the most abundant biopolymer on Earth and can be extracted from sources such as higher plants, algae, and, to a lesser extent, from tunicates and bacteria (Habibi et al., 2010; Zhao & Li, 2014). Cellulose is characterized by a hierarchical structure in which cellulose chains aggregate to form nanofibrils with alternating crystalline and less-organized domains. The interactions between the chains are mainly governed by the presence of hydrogen bonds between the hydroxyls lying in the glucose unit ring plane, and Van der Waals interactions out of the ring plane. Cellulose typically occurs in two native crystalline forms, namely Iα and Iβ, characterized by parallel-oriented chains and collectively referred to as cellulose I (Salem et al., 2023; Sèbe et al., 2012). Another allomorph of significant scientific and industrial relevance is cellulose II, which is composed of antiparallel glycosidic chains (Flauzino Neto et al., 2016; Sèbe et al., 2012). This form is thermodynamically more stable than the allomorph I and is typically obtained from native cellulose through irreversible processes called mercerization and regeneration (Hubbe et al., 2024; Sharma et al., 2015) Mercerization is a solid-state process, where native cellulose is swollen in a concentrated sodium hydroxide solution and recrystallizes into cellulose II upon removing the swelling agent.(Meurs

* Corresponding author.
E-mail address: alessandra.vitale@polito.it (A. Vitale).

https://doi.org/10.1016/j.carpta.2026.101125

Available online 21 March 2026

et al., 2026) Regeneration, instead, is a process where the conversion is achieved by solubilization of cellulose in a solvent, followed by its reprecipitation in water (O"sullivan, 1997; Phanthong et al., 2018; Shibazaki et al., 1997). Other cellulose allomorphs (III_I, III_{II}, IV_I, IV_{II}, and X) have been identified, but their relevance is mostly academic (Salem et al., 2023).

Over the last few decades, the exponential growth of nanosciences has brought attention to the development of nanomaterials derived from cellulose. This class of materials, commonly reported as nanocellulose (NC), is generally characterized by a high tensile modulus, a large surface area, and complete renewability (Amara et al., 2021; Thomas et al., 2018). Cellulose nanofibrils (CNFs) and cellulose nanocrystals (CNCs) are two primary forms of NC. CNCs are commonly described as rod-like particles with a width typically between 3 and 50 nm and a length between 100 nm and several micrometers, resulting in a form factor usually falling within the 5–50 range (ISO Standard TS 23151:2021). Due to their low density and their impressive mechanical properties, CNCs have found applications in different fields, including polymer nanocomposites, biodegradable food packaging, and electronics (Amara et al., 2021; Shojaeiarani et al., 2021). The properties and potential applications of CNCs are influenced by their shape and dimensions, which in turn strongly depend on the source of cellulose and the preparation method (Babaei-Ghazvini et al., 2024; Brito et al., 2012; Leong et al., 2022; Song et al., 2019; Yu et al., 2021). For example, crystals with a high aspect ratio are usually preferred for mechanical reinforcement thanks to their ability to form a percolated network at a low filler volume fraction, while low-aspect ratio CNCs could be used to enhance gas barrier properties in nanocomposites (Babaei-Ghazvini et al., 2024; Leong et al., 2022).

In the literature, many sources of cellulose have been used for the preparation of CNCs, while the processing is typically an acid hydrolysis carried out between 45 and 65 °C, for up to 90 min (Chen et al., 2015; Leong et al., 2022; Tang et al., 2022). Sulfuric acid is the most commonly employed hydrolyzing agent, although other acids, such as hydrochloric, oxalic, maleic, and phosphotungstic acids, have also been reported (Filson & Dawson-Andoh, 2009; Jia et al., 2017; Liu et al., 2014; Pawcenis et al., 2022). Sulfuric acid selectively degrades the disorganized regions of cellulose nanofibrils, while preserving the crystalline domains. The resulting CNCs have anionic sulfate ester groups on their surface, ensuring their colloidal stability in aqueous media (Sarı & Kaynak, 2025).

The present study investigates the sulfuric acid hydrolysis of cellulose from different sources under room-temperature conditions. While the study of the morphology of CNCs produced at varying acid concentrations has been extensively reported, room-temperature hydrolysis has so far received limited attention (Song et al., 2019; Wang et al., 2012; Yu et al., 2021). Previous studies have established that the hydrolysis severity strongly influenced the CNC yield and properties, with sulfuric acid concentration generally exerting a more dominant effect than temperature or time under conventional conditions (Chen et al., 2015). However, hydrolysis parameters can also direct recrystallization pathways and crystalline polymorphism, suggesting that temperature suppression may promote alternative structural evolution routes.

In addition to assessing the influence of the cellulose origin, the effect of a mercerization pretreatment prior to hydrolysis is examined to elucidate how composition, crystalline polymorphism, and mercerization-induced swelling jointly affect the structure of the resulting CNCs. Mercerization not only converts cellulose I into cellulose II but also increases fiber accessibility and porosity, which are expected to influence hydrolysis kinetics (Lin et al., 2022). Particular attention is devoted to the CNC morphology, analyzed by transmission electron microscopy (TEM), with the aim of identifying structure–processing relationships. Rather than benchmarking efficiency against conventional high-temperature protocols, this study exploits suppressed thermal activation as a structure-directing regime to access unconventional hierarchical and flake-like CNC morphologies. Although related nanostructures have been sporadically observed under mild hydrolysis conditions, a systematic investigation of how cellulose origin, mercerization pretreatment, and crystalline polymorphism jointly influence nanocrystal morphology under a room-temperature hydrolysis regime remains lacking. In this context, the present work explored this unusual strategy to access distinctive NC morphologies and provide experimental insights toward a deeper understanding of the formation of hierarchical nanostructures.

2. Materials and methods

2.1. Materials

Dried sheets of delignified and bleached hemp fibers were provided by OP Papírna, s.r.o. (Czech Republic). Commercial micronized (6–12 μm) and delignified wood pulp (Technocel FM8) was provided by CFF GmbH & Co (Germany). Microfibrillated cellulose paste (Exilva P01V), derived from Norwegian spruce, was kindly provided by Borregaard (Norway). In the following, these materials will be referred to as hemp pulp (HP), microfibrillated cellulose (MFC), and micronized cellulose powder (MCP), respectively. H_2SO_4 and NaOH were purchased from Sigma-Aldrich. All the materials were used without further purification.

2.2. Mercerization

Native cellulose (1.5 g) was treated in 30 mL of a 20 wt% NaOH solution for 5 h at room temperature. The suspension was then diluted 10 times using deionized water and was vacuum filtrated using a 0.20-μm cellulose nitrate membrane filter by Advantec MFS. The mercerized cellulose was then rinsed multiple times on the filter using deionized water.

2.3. CNC extraction

Cellulose (1.5 g) was treated in 90 mL of a 64 wt% solution of H_2SO_4 under stirring. The extraction proceeded under stirring for 2 h at room temperature (25°C). The reaction mixture was subsequently diluted 3 times using cold distilled water and allowed to rest for 1–2 h to allow cellulose to sediment. The supernatant was removed, and the suspension/decanting processes were repeated two more times. The CNC mixture was partially neutralized with NaOH until reaching pH 1 and dialyzed against distilled water using a 14 kDa membrane (Sigma-Aldrich), until the dialysis bath reached the conductivity value of distilled water. The resulting suspension was sonicated for 30 min at 30% amplitude with a TS103 tip of a Bandelin Sonoplus 400 W, followed by filtration using a 0.65 μm cellulose ester membrane filter (Advantec MFS) to remove large aggregates. The extraction process was performed on both native and mercerized materials.

2.4. X-ray diffraction (XRD)

XRD patterns were collected on nanocellulose samples using a Malvern Panalytical Empyrean diffractometer equipped with CuKα radiation (λ = 0.15418 nm) and a PIXcel 3D solid-state detector with rapid readout and high dynamic range. Measurements were performed at 40 kV and 40 mA over a 2θ range of 10–40°, with a step size of 0.02°. A Bragg–Brentano High Definition (BBHD) optic was used on the incident beam to improve resolution and enable more reliable quantification of the amorphous contribution. For comparative evaluation of crystallinity, the crystallinity index (CI) was calculated using Segal's method (Segal et al., 1959; Park et al., 2010):

$$CI = 100 \times \frac{(I_{cr} - I_{am})}{I_{cr}} \quad (1)$$

where I_{cr} corresponds to the maximum intensity of the (200) reflection

for cellulose Iβ or the (110) reflection for cellulose II, and I_{am} represents the intensity associated with the amorphous fraction, taken as the minimum intensity between the (200) and (110) peaks of cellulose Iβ (2θ ≈ 18°) or between the (110) and ($1\bar{1}0$) peaks of cellulose II (2θ ≈ 15°), respectively (Park et al., 2010). The CI values are intended for relative comparison between samples.

The crystallite size was estimated using Scherrer's equation by analyzing the full width at half maximum (FWHM) of selected reflections after correction for instrumental broadening (Scherrer, 1918):

$$D_{hkl} = \frac{K\lambda}{\beta \cos\theta_{hkl}} \quad (2)$$

where D_{hkl} is the crystallite size perpendicular to the (hkl) planes, K is the shape factor (typically close to unity), λ is the X-ray radiation wavelength, β is the corrected FWHM (in radians), and θ_{hkl} is the Bragg angle.

Peak profile fitting was performed using High Score Plus software (Malvern Panalytical) with pseudo-Voigt functions (Kα1/Kα2 splitting) on background-subtracted patterns. Instrumental broadening was determined using LaB_6 standard powder (NIST SRM®660a, crystallite size within the 2–5 nm range) and subtracted from measured peak widths.

2.5. Electron microscopy

Native samples were analyzed by SEM. The dry powders were deposited on conductive carbon tape and coated with platinum using a Quorum Q150T ES Pt sputter coater. The specimens were observed with a Zeiss Supra 40 scanning electron microscope (SEM) equipped with a field emission (FE) gun, and operating at 3 kV, in secondary electron imaging mode.

In addition, CNC suspensions were characterized by TEM. Droplets of ca. 0.001 wt% suspensions were deposited onto freshly glow-discharged carbon-coated grids and negatively stained with 2 wt% uranyl acetate. The specimens were observed with a Jeol JEM-2100 Plus microscope operating at 200 kV, and images were recorded with a Gatan Rio 16 camera. The particle size was measured from the FE-SEM and TEM micrographs using the ImageJ software. The average values of length, width, and aspect ratio were calculated after measuring 200 particles from each sample.

2.6. Fourier-transform infrared spectroscopy (FT-IR)

Oven-dried cellulose samples were dispersed in KBr, and their FT-IR spectra were collected in transmission mode using a Nicolet iS50 FT-IR spectrometer by Thermo Scientific, with a 4 cm^{-1} resolution and a total of 32 scans per sample.

2.7. Dynamic light scattering (DLS) and ζ -potential

DLS analyses and ζ-potential measurement were performed on 0.01 wt% CNC aqueous suspensions at pH 8 using a Litesizer 500 by Anton Paar GmbH. ζ-potential measurements were performed at pH 8, through the same DLS device (Litesizer 500, Anton Paar) equipped with an Omega Cuvette.

2.8. Sugar composition analysis

The quantification of fucose, arabinose, rhamnose, glucose, galactose, mannose, xylose, ribose, glucuronic acid, and galacturonic acid was performed on the native starting materials by anionic liquid chromatography. The samples were previously hydrolyzed in concentrated sulfuric acid and then analyzed using a DIONEX ICS6000, equipped with a CarboPac PA1 (250 × 2 mm) column and a PAD detector. The cellulose, glucomannan, and xylan contents were estimated using the method described by Zhu & Theliander (2015).

2.9. Elemental analysis

The moles of $–OSO_3H$ groups of the CNC samples per 100 glucose units (n) were calculated through the method reported by Hu et al. (2014)), using the formula:

$$n = \frac{100 \times 162.14 \times S\%}{[32.07 - (80.06 \times S\%)]} \quad (3)$$

where *S* is the weight percentage of sulfur determined by elemental analysis performed with the CHNS elemental analyzer vario Macro cube by Elementar Analysensysteme GmbH (Germany).

3. Results and discussion

3.1. Characterization of the cellulosic starting materials

HP, MCP, and MFC were selected to establish a quantitative baseline for assessing the effects of source and pretreatment on the CNC preparation. These materials differ in botanical origin and initial morphology, enabling a systematic comparison of their chemical composition, crystallinity, crystallite size, and fiber dimensions prior to hydrolysis. The quantitative sugar compositions of the native starting materials are reported in Table 1. All samples exhibit a total hemicellulose content lower than 10 wt%. HP contains both glucomannan and xylan, which are the main constituents of the hemicellulosic fraction in hemp, in agreement with previous studies (Buchert et al., 1994; Gaynor et al., 2024). In MCP, only xylan was observed, while the presence of glucomannan was not detected, consistent with its origin from hardwood feedstock (Buchert et al., 1994; Pérez et al., 2002). In contrast, MFC from Norwegian spruce exhibits a higher amount of glucomannan compared to xylan. These values are consistent with the literature, where glucomannan is reported as the predominant hemicellulose component in softwoods (Buchert et al., 1994; Pérez et al., 2002).

Moreover, an alkali treatment (mercerization) was conducted on a dilute (around 1.6 wt%) suspension of pristine HP, MCP, and MFC, resulting in their mercerized counterparts. A schematic representation of the mercerization process is illustrated in Scheme 1a. The mass yields of the mercerized samples, calculated after drying, were 94, 92, and 90% for HP, MCP, and MFC, respectively. As a result, six distinct cellulosic materials were used as starting materials to prepare CNCs: native HP, MCP, and MFC, along with their mercerized forms (i.e., merc. HP, merc. MCP, and merc. MFC).

The morphology of both native and mercerized cellulose samples was characterized by FE-SEM observation (Fig. 1). In addition to qualitative morphological differences, quantitative estimates of fiber width, length, and aspect ratio were obtained, providing comparative metrics for the different starting materials. HP fibers (Fig. 1a) exhibit a wide diameter distribution, ranging from tens of μm to hundreds of nm. The native MCP appears composed of particles (Fig. 1b) characterized by an average aspect ratio lower than 3 (specifically, 2.7 ± 1.0). >50% of the particles exhibit a length lower than 20 μm. MFC is in the form of interwoven micro- and nanofibrils, resulting in a film with a homogeneous surface (Fig. 1c). All the analyzed fibrils exhibit a diameter well below 1 μm, with a mean value of 130 ± 90 nm.

Mercerized HP (Fig. 1d) is characterized by fibers with a width distribution comparable to that of native HP. Mercerized MCP (Fig. 1e)

Table 1
Polysaccharide compositions of the native starting materials.

Starting material	Cellulose (wt%)	Glucomannan (wt%)	Xylan (wt%)
HP	95.2	2.0	2.8
MCP	97.4	0	2.6
MFC	90.9	7.6	1.5

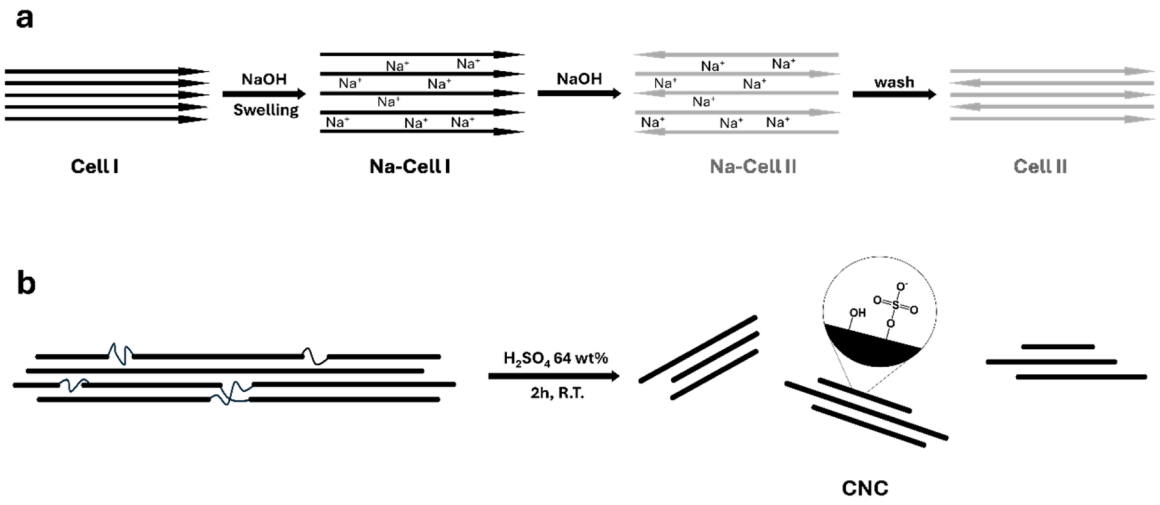

Scheme 1. Graphical representation of cellulose mercerization (a) and of CNC extraction (b). The arrows represent the direction of the chain in the two allomorphs: cellulose I (parallel) and cellulose II (antiparallel).

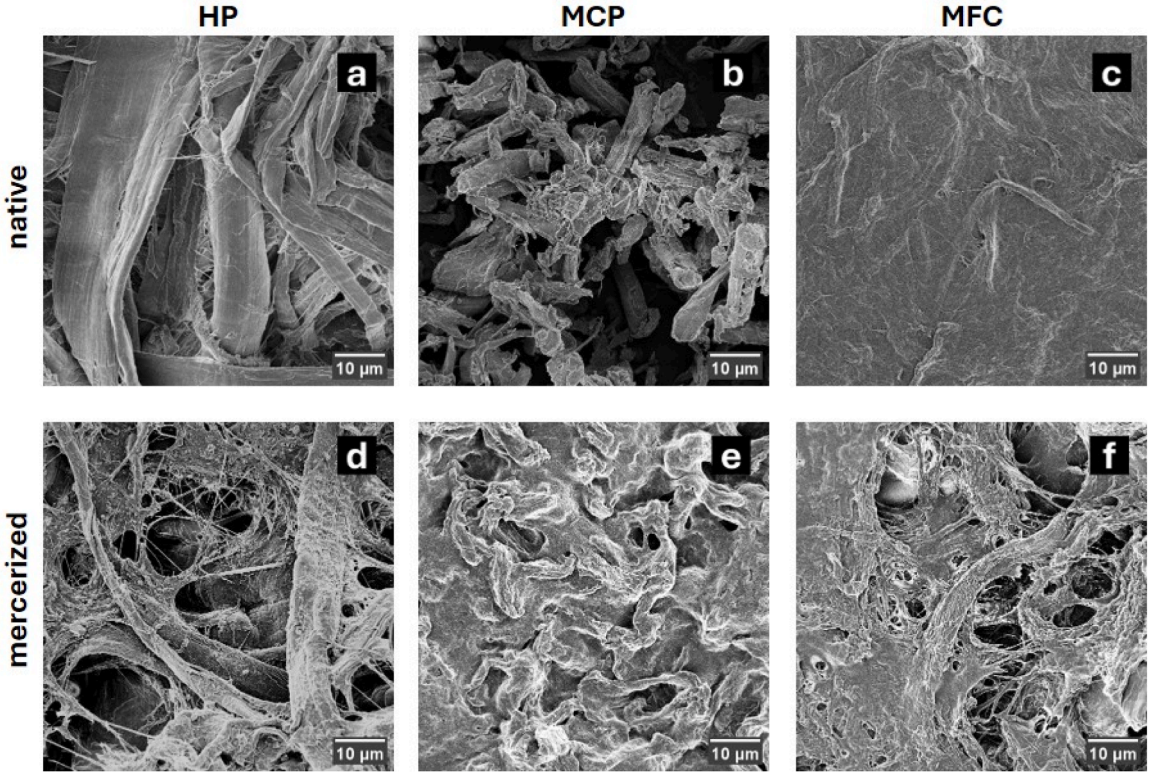

Fig. 1. FESEM micrographs of the different starting cellulosic materials used for the preparation of CNCs: HP (a), MCP (b), MFC (c), merc. HP (d), merc. MCP (e) and merc. MFC (f).

appears similar to the corresponding native material, but with a slightly reduced aspect ratio (2.4 ± 1) and average length (14 ± 4 µm) of particles. Mercerized MFC is shown in Fig. 1f: the sample appears less homogeneous and compacted than the native material and shows the presence of nanofibers with nanometric width together with some micrometric bundles. In both mercerized and native MFC and HP samples, it was not possible to estimate the average aspect ratio of the fibers due to their overlapping and their high length.

The crystalline structure, crystallinity index, and crystallite size, used here as semi-quantitative descriptors of supramolecular organization, were analyzed by XRD, and the results are reported in Fig. 2a and Table 2. The diffraction patterns of the native starting materials exhibit the four characteristic reflections of cellulose Iβ at $2\theta = 15.0°$, 16.5°, 22.5°, and 34.5° (French, 2014; Gong et al., 2017). The first three reflections correspond to the $(1\bar{1}0)$, (110) and (200) crystal planes, respectively, while the weak signal at 34.5° is due to the overlapping of several minor higher-order reflections. Moreover, in the MCP and MFC profiles, a shoulder at approximately $2\theta = 20.5°$, related to the (012) and (102) planes, is also present (French, 2014). This feature is not clearly visible in the HP pattern, likely due to preferred orientation effects in the dried fibrous sample (French, 2014).

Following mercerization, the diffraction profiles of HP, MCP, and MFC exhibit the characteristic pattern of cellulose II, with reflections at

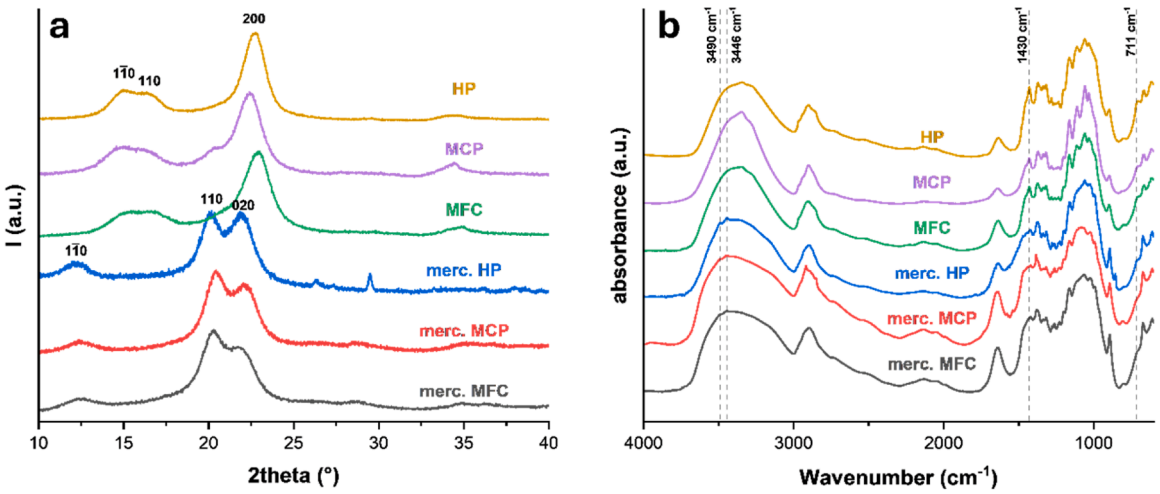

Fig. 2. XRD profiles (a) and FT-IR spectra (b) of the six starting materials.

Table 2
XRD 2θmax values of cellulose I and cellulose II, crystallinity index (CI), and crystallite size of the six starting materials.

Sample	2θ Cellulose I I_{200} (±0.05°)	2θ Cellulose II I_{110} (±0.05°)	CI (%)	Crystallite size (Å)
HP	22.63		89	58
MCP	22.28		86	47
MFC	22.76		84	44
merc. HP		20.08	23*	64
merc. MCP		20.40	64*	58
merc. MFC		20.20	44*	62

* Values referred only to cellulose II.

approximately 12.0°, 20.5°, and 22.0° corresponding to the (1$\bar{1}$0), (110), and (020) crystal planes, respectively (French, 2014; Gong et al., 2017). The disappearance of the cellulose Iβ reflections at 15–17° confirms the conversion from cellulose I to cellulose II upon alkaline treatment. Polymorph identification was primarily based on peak positions and profile evolution rather than CI values alone.

The CIs calculated from the XRD profiles using Segal's method are reported in Table 2. The CI values are intended for relative comparison between samples rather than absolute quantification of crystalline fractions. Native HP, MCP, and MFC exhibit similar CIs, with values ranging from 84 to 89%, consistent with their cellulose Iβ structure. After mercerization, all samples show the emergence of cellulose II reflections accompanied by a decrease in apparent CI values. This decrease in apparent crystallinity caused by mercerization has been previously reported and is attributed to structural rearrangement and increased disorder during the I-to-II polymorphic transition, particularly in highly crystalline substrates (Halonen et al., 2013; Haouache et al., 2022; Revol et al., 1986; Yue et al., 2013).

The FT-IR spectra of the native and mercerized starting materials (Fig. 2b) exhibit the characteristic peaks of cellulose. However, subtle differences in the spectra reflect variations in the crystalline structure of the materials. In particular, analysis of the -OH stretching band, which appears in any cellulosic samples between 3000 cm^{-1} and 3600 cm^{-1}, reveals two weak peaks at 3490 cm^{-1} and 3446 cm^{-1} that are exclusively present in the mercerized samples. These signals are associated with the intramolecular hydrogen bonding of cellulose II, confirming the crystallographic change due to mercerization observed by XRD. Furthermore, the spectra of the mercerized samples do not show the peak at 711 cm^{-1}, related to cellulose Iβ, which is evident in the native materials, in agreement with diffraction results (Zuluaga et al., 2009).

The decrease in the intensity of the peak at 1427 cm^{-1}, attributed to symmetric –CH_2 bending, and a shift of the signal corresponding to C-O-C vibration of the glycosidic bond from 898 to 894 cm^{-1} are also observed: these features have already been reported in the literature for mercerized materials and are attributed to conformational change from the *tg* to *gt* form of the CH_2OH and by the different torsional angles of β-(1-4)-D-glycosidic bond, respectively (Dhar et al., 2015; Flauzino Neto et al., 2016; Han et al., 2013; Ray & Sarkar, 2001).

Although XRD and FT-IR data confirmed the conversion of cellulose I to cellulose II after mercerization, they did not capture the associated swelling-induced changes in accessibility that are known to influence acid hydrolysis. Consequently, polymorphic transition and increased accessibility are treated here as concomitant, non-separable contributors to the observed behavior.

3.2. Characterization of the extracted CNCs

CNCs were extracted from both the native and mercerized starting materials according to Scheme 1b. Acid hydrolysis was performed with H_2SO_4 as widely reported in the literature, but operating at room temperature, without external heating. It should be noted that the room-temperature conditions adopted in this study require a higher acid-to-cellulose ratio and longer reaction times than conventional sulfuric acid hydrolysis conducted at elevated temperatures. A sulfuric acid concentration of 64 wt% was selected, consistent with widely adopted literature protocols, in order to isolate the effect of suppressed thermal activation without introducing acid-strength as an additional variable.

After extraction, translucent water suspensions with concentrations ranging from 0.7 to 1.5 wt% were obtained. The extraction mass yields, the sulfur content, the estimation of sulfate ester groups calculated from the elemental analysis, and the average ζ -potential of CNCs from native and mercerized starting materials are summarized in Table 3. The yields

Table 3
Mass yield of CNC extraction, sulfur content, number of –OSO_3H groups per 100 glucose units (n), and average ζ -potential of CNCs from native and mercerized starting materials.

	Starting material	CNC mass yield (%)	Sulfur content (%)	n	ζ-potential (mV)
native	HP	54	0.50	2.58	-33
	MCP	46	0.24	1.24	-29
	MFC	45	0.69	3.53	-34
mercerized	merc. HP	62	0.89	4.62	-28
	merc. MCP	55	1.77	9.37	-36
	merc. MFC	44	1.19	6.19	-28

range from 44 to 62 wt% and are consistent with the data already reported in the literature for sulfuric acid extractions from different sources (Leong et al., 2022; Tang et al., 2022). The CNCs extracted from mercerized materials exhibited a higher sulfur content and a greater number of $–OSO_3H$ groups compared to their native counterparts, which are characterized by content values consistent with previous reports in literature for CNCs extracted at 35°C (Chen et al., 2015). This behavior is consistent with the pronounced swelling induced by mercerization, which increases surface accessibility and the density of reactive sites (Ferro et al., 2020; Kalia et al., 2009), thereby enhancing susceptibility to sulfate ester grafting during acid hydrolysis (Li et al., 2024).

The colloidal stability of the CNC suspensions was evaluated by ζ-potential measurements (Table 3). All the samples exhibit potential within the range between -28 and -36 mV at pH = 8. These negative values confirm the introduction of anionic sulfate ester groups on the surface of the crystals during the extraction procedure, in agreement with the literature (Abitbol et al., 2013; Reid et al., 2017). The absolute ζ-potential values ($|\zeta| > 20$ mV) exceed the threshold generally considered necessary to ensure moderate colloidal stability (Bhattacharjee, 2016). Consistently, the CNC suspensions did not exhibit flocculation or precipitation phenomena during a 6-month storage (**Figure S1** of the Supporting Information).

The size distribution and the average hydrodynamic diameters of the CNCs were analyzed in aqueous suspension by DLS. A monomodal size distribution centered below 200 nm was observed in all the extracted samples (**Figure S2** and **Table S1**), confirming the nanometric dimension of the particles (Bhattacharjee, 2016; Tarrés et al., 2022).

The TEM images of the samples after hydrolysis of the six starting materials are compared in Fig. 3 (size distributions determined from TEM images, additional images, and enlarged insets of Fig. 3 are provided in **Figures S3** and **Figure S4 of the Supporting Information**). CNCs derived from native HP (Fig. 3a) exhibit the typical morphology of cellulose I nanocrystals, consisting of rod-like particles with an average length of 218 ± 67 nm and an average width of 18 ± 6 nm. Higher magnification micrographs (Fig. 3a and **S2d**) reveal that these CNCs are composed of thinner laterally-bound crystallites. Their size and morphology appeared consistent with the hemp-derived CNCs obtained using H_2SO_4 at higher hydrolysis temperatures, as reported in the literature (Bahsaine et al., 2023; Luzi et al., 2014; Najafi & Kahyaoglu, 2024). Furthermore, a few kinked particles, with a length higher than 1 μm and a width of a few nm, were also observed (**Figure S3d**). Similar defects have been previously reported in the literature and are probably caused by residual disorganized regions between crystalline domains (Camargos & Rezende, 2021; Leong et al., 2022). The nanocellulose extracted from merc. HP (Fig. 3d) exhibits shorter nanocrystals (146 ± 44 nm) with a higher average width (27 ± 10 nm) compared to those obtained from native HP. The lower length and aspect ratio of CNCs from mercerized material are consistent with the observations reported for CNCs extracted from native and mercerized eucalyptus cellulose (Flauzino Neto et al., 2016).

A markedly different morphology was observed for the CNCs extracted from native MCP and MFC (Fig. 3b and c). Both samples appeared to contain two distinct particle populations, differing in size and shape. The smaller population, visible at higher magnification (**Figures S2e** and **S2f**), consists of particles with an average length of about 45 nm. In contrast, the larger population exhibits average lengths of around 330 nm and appears as long rod-like particles decorated with ribbon-like surface features (Fig. 3b and c). Similar ribbon-like structures were also observed as isolated entities (**Figure S3e**). The morphology of these smaller particles resembles that of the particles reported by Neto et al., obtained through a relatively low-temperature (40°C) acid treatment and referred to as "regenerated CNCs" (Flauzino Neto et al., 2016). The authors showed that in these cellulose II particles, the short cellulose chains were indeed packed perpendicularly to the long axis of the ribbons, contrary to the cellulose I nanocrystals in which the chains were parallel to the long axis. Consequently, the width of the ribbon should correspond approximately to the length of the cellulose chains. The surface-decorating features of the CNCs are hypothesized to

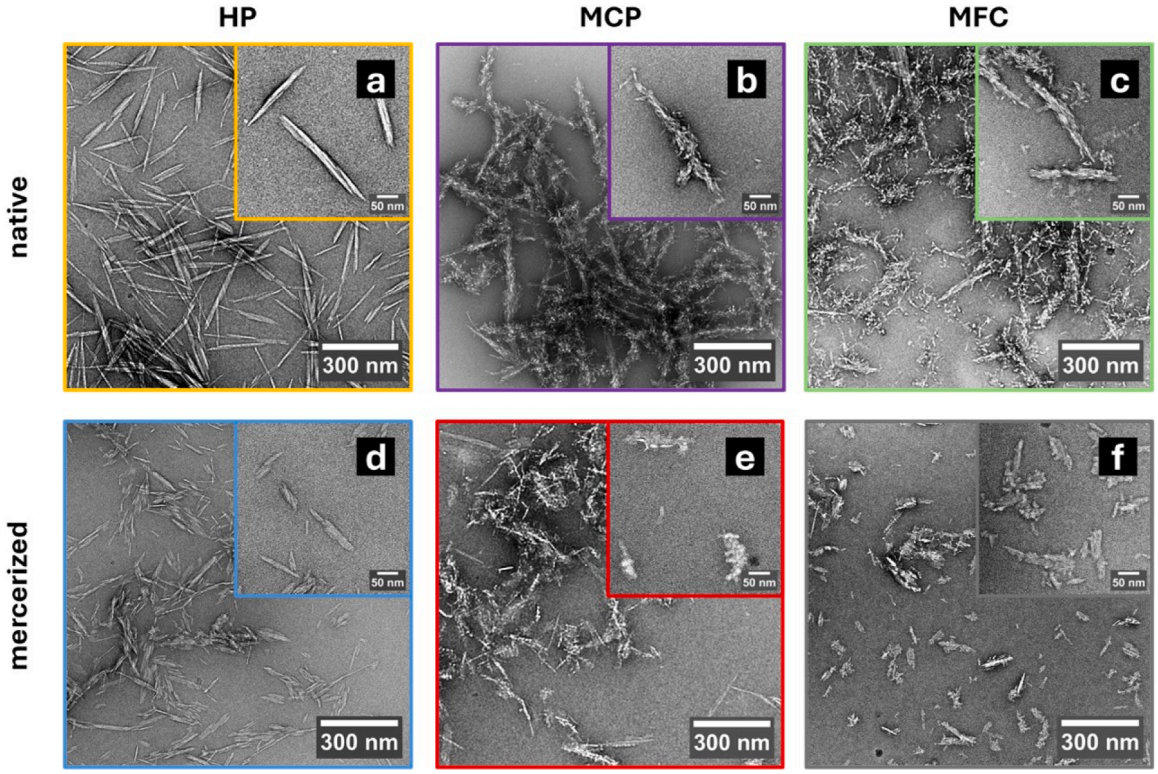

Fig. 3. TEM micrographs of negatively stained CNCs extracted from native HP (a), native MCP (b), native MFC (c), merc. HP (d), merc. MCP (e) and merc. MFC (f). Insets: enlarged views of some characteristic particles.

be made of cellulose oligosaccharides that precipitated during the purification process, as previously reported (Bouchard et al., 2016; Niinivaara et al., 2021). The average width of these smaller particles is approximately 15 nm and is consistent with the value of 12 nm measured by Neto et al. for regenerated cellulose II ribbons, characterized by a relatively low DP of 17 (Flauzino Neto et al., 2016).

For usual hydrolysis conditions (i.e., at 65°C), a significant fraction of cellulose is converted into mono and oligosaccharides. Oligomers with a degree of polymerization (DP) lower than 6 are soluble in water and can be removed from CNCs during dialysis (Taylor, 1957; Niinivaara et al., 2021), while oligosaccharides with higher DP chains are only soluble in concentrated acid solutions. At lower temperatures, hydrolysis kinetics are slower, favoring the formation of larger oligosaccharides that can precipitate upon dilution of the acid during purification and are not removed by the subsequent dialysis (Bouchard et al., 2016; Niinivaara et al., 2021). Although this behavior could be interpreted as incomplete hydrolysis when judged against conventional protocols, it instead reflects a distinct hydrolysis–recrystallization pathway enabled by suppressed thermal activation. In this kinetic regime, the persistence and controlled deposition of oligosaccharides become integral to nanostructure formation rather than an experimental artefact, leading to hierarchical, surface-decorated CNCs instead of neat nanocrystals. Such oligosaccharide-coated CNCs have been shown to exhibit modified physicochemical properties, including altered surface chemistry and charge density, reduced water adsorption capacity, and lower viscosity, and have been proposed as a viable surface modification strategy rather than a limitation (Bouchard et al., 2016; Niinivaara et al., 2021). Therefore, the controlled deposition of oligosaccharides represents a promising surface modification method with the potential of becoming an industrially relevant process, and the hierarchical and surface-decorated CNCs observed in the present study should be regarded as structurally distinct nanomaterials generated through a specific kinetic regime.

The presence of two populations of particles was also observed for CNCs extracted from mercerized MCP (Fig. 3e). In this case, however, the smaller population appears to consist of aggregates formed by randomly oriented fragments, rather than small ribbon-like structures as described above for native MCP and MFC.

The CNCs obtained from mercerized MFC (Fig. 3f) exhibit only one population of particles, having an average length smaller than that of the corresponding non-mercerized sample (115 ± 47 nm). These particles have an unusual flake-like shape, distinctly different from the typical rod-like shape of CNCs and appear to be composed of irregularly aggregated smaller fragments. To the best of our knowledge, CNCs exhibiting such flake-like morphologies obtained directly by sulfuric acid hydrolysis, without post-treatment steps, have not been previously reported. Although similar compact cellulose II nanocrystals were obtained via oxalic acid hydrolysis of microfibrillated dissolving pulp, the present results indicate that this morphology is not solely dictated by acid chemistry. Suppressed thermal activation under sulfuric acid conditions can likewise promote distinct fragmentation–reassembly pathways and polymorphic transitions (Jia et al., 2017).

The relatively narrow size distribution and reproducible morphology of the CNCs from mercerized MFC indicate that they are not the result of random aggregation during drying or sample preparation. Instead, their formation is attributed to a distinct fragmentation–reassembly pathway activated under the combined effects of low crystallinity, mercerization-induced swelling, and suppressed hydrolysis kinetics. Under these conditions, fragmentation and reassembly pathways distinct from those operating under conventional hydrolysis conditions are promoted, and partial depolymerization and limited recrystallization appear to favor the formation of compact, plate-like assemblies rather than elongated rod-like nanocrystals.

It is important to notice that native MFC and MCC yielded particles with analogous morphologies, whereas their mercerized counterpart did not. This behavior may be attributed to the combined effects of mercerization-induced swelling and cellulose II formation, which together increase acid accessibility and modify hydrolysis and recrystallization pathways. In particular, the lower crystallinity of mercerized MFC (Table 2) likely enhanced its susceptibility to the concentrated acid environment, promoting more extensive fragmentation.

Although the hybrid CNCs obtained from native MCP and MFC and flake-like CNCs obtained from mercerized MFC differ in morphology, both are proposed to originate from a related kinetic regime characterized by slow hydrolysis and the persistence of intermediate cellulose fragments. In the former case, higher-crystallinity substrates would favor partial preservation of rod-like cores decorated by recrystallized oligosaccharides, whereas in the latter case, lower crystallinity and higher accessibility favor more extensive fragmentation and reassembly into compact flake-like structures.

Although negative staining may potentially introduce imaging artifacts, the observed morphologies were consistently reproduced across multiple independently prepared samples and grids, indicating that these structural features are intrinsic to the material rather than artifacts arising from staining or drying.

The average particle dimensions determined by TEM micrographs for all six investigated samples are reported in **Table S2**. Differences between TEM-derived size distributions and dimensions and DLS results (**Table S1**) arise from intrinsic limitations of DLS, which cannot distinguish individual particles from aggregates and is dominated by larger scattering species, while also assuming spherical particle geometry (Bellmann et al., 2019). The comparatively narrow size distribution observed for flake-like CNCs further supports a kinetically controlled formation mechanism, as random aggregation would be expected to yield broader, poorly reproducible size distributions.

The crystalline structure of the extracted CNCs was analyzed by XRD, and the corresponding diffraction profiles are reported in Fig. 4a. The XRD analysis revealed several differences in the crystalline forms of CNCs extracted from the native starting materials. The HP CNCs preserved the same crystalline form of hemp pulp, exhibiting the characteristic pattern of cellulose Iβ. The diffraction profiles of CNCs extracted from MCP and MFC showed, instead, diffraction patterns predominantly associated with cellulose II, with weak residual reflections in the 2θ range between 15 and 17°, indicating the presence of remaining cellulose Iβ domains. These features suggest that partial conversion from cellulose I to cellulose II occurred during acid hydrolysis. The formation of cellulose II nanocrystals from non-mercerized starting materials has been previously reported and attributed to dissolution-recrystallization phenomena during processing (Flauzino Neto et al., 2016; Haafiz et al., 2014; Sèbe et al., 2012; Xing et al., 2018). In the present case, this behavior is likely promoted by the low hydrolysis temperature, which, as previously described, promotes the formation and solubilization of large oligosaccharides (DP > 6) that can recrystallize into the more thermodynamically stable cellulose II form during dilution and purification (Flauzino Neto et al., 2016; Hattori et al., 2012). As expected, all the CNCs extracted from mercerized cellulose substrates exhibited diffraction profiles characteristic of cellulose II (Fig. 4a). However, the CNCs derived from mercerized HP show comparatively lower relative intensities of cellulose II reflections. This is likely attributable to preferred orientation (texture) effects arising from particle morphology and film deposition during sample preparation. Therefore, the reduced peak intensity can be interpreted as an orientation effect rather than a decrease in crystallinity.

The CI values of the extracted CNCs are reported in Table 5. Acid hydrolysis resulted in an increase in apparent CI for HP, merc. HP, and merc. MFC, whereas no significant change was observed for mercerized MCP. Preferential degradation of amorphous regions during hydrolysis is expected to increase apparent crystallinity. Conversely, severe hydrolysis conditions may induce partial disruption of crystalline domains, limiting CI enhancement (Chanthathamrongsiri et al., 2021). Thus, the variations observed among samples likely reflect differences in substrate sensitivity to hydrolysis conditions (Leong et al., 2022), as well as

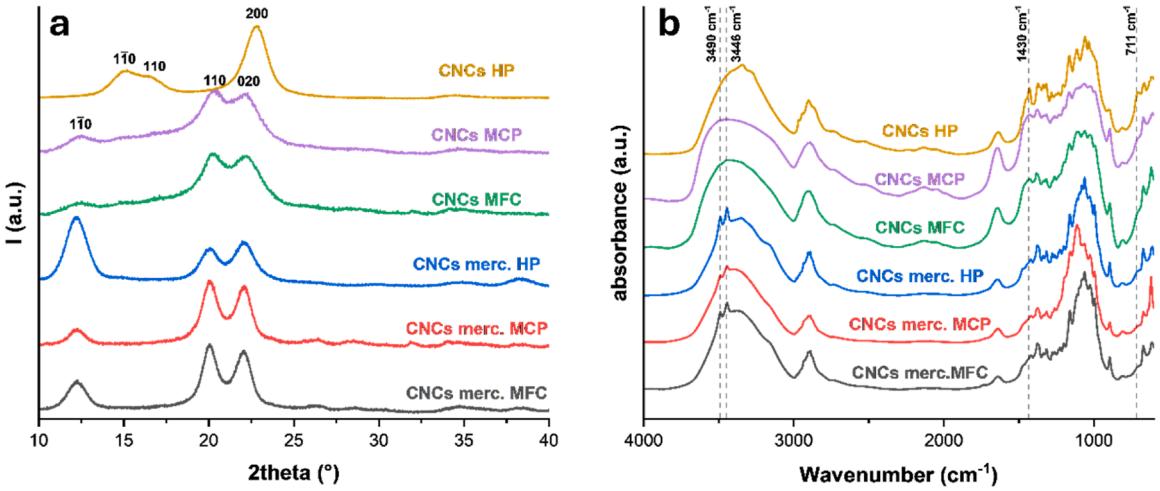

Fig. 4. XRD diffraction profiles (a) and FT-IR spectra (b) of CNCs extracted from native HP, native MCP, native MFC, and merc. HP, merc. MCP and merc. MFC.

Table 5
XRD $2\theta_{max}$ values of cellulose I and II, degree of crystallinity (CI), and crystallite size of CNCs.

Starting material	2θ Cellulose I I_{200} (±0.05°)	2θ Cellulose II I_{110} (±0.05°)	CI (%)	Crystallite size (Å)
HP	22.71		91	57
MCP	22.15	20.21	61*	42
MFC	22.26	20.23	64*	44
merc. HP		20.01	32*	72
merc. MCP		20.05	64*	79
merc. MFC		20.05	66*	88

* Values referred only to cellulose II.

potential texture effects influencing diffracted intensity.

The FT-IR spectra of the extracted CNCs are shown in Fig. 4b. As previously discussed, the -OH stretching band of CNCs derived from mercerized materials displays the two characteristic peaks at 3490 and 3446 cm^{-1}, related to cellulose II. Moreover, all spectra, except the one of CNCs from native HP, show a decrease of the intensity of the peak at 1427 cm^{-1} and the disappearance of the signal at 711 cm^{-1}. In contrast, CNCs from native HP still show the signal at 711 cm^{-1}, with no evidence of cellulose II (vibrational bands at 3490 cm^{-1} and at 3446 cm^{-1}), confirming the absence of crystallographic conversion from form I to form II, in agreement with the XRD results.

A schematic representation of the obtained nanoparticles is shown in Scheme 2, where the different morphologies are reported along with their respective cellulose sources and crystalline structures.

4. Conclusions

This study demonstrates that CNCs can be successfully produced by acid hydrolysis performed at room temperature, using cellulose from

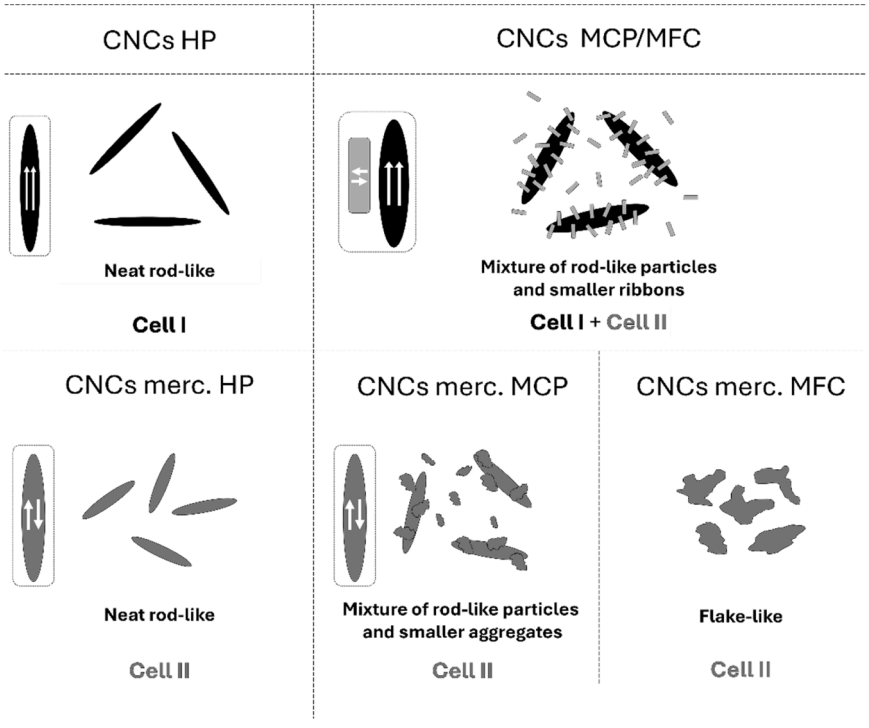

Scheme 2. Graphical representation of the morphologies and crystalline structures obtained in this work from the different native and mercerized sources.

different sources (i.e., HP, MCP, and MFC), in both native and mercerized forms. Interestingly, the process yielded CNCs characterized by relevant differences in size, shape, and crystalline structure, depending on the cellulose source and pretreatment. Hydrolysis of native hemp pulp produced nanocrystals characterized by the typical rod-like shape and the structure of cellulose I, while mercerized hemp pulp yielded similar morphologies in the cellulose II form. In contrast, nanocelluloses extracted from native MFC and MCP appeared to consist of a mixture of cellulose I and cellulose II nanoparticles, even if the materials were not subjected to the alkaline environment of mercerization. Based on comparison with the existing literature, the presence of cellulose II form in these samples may be attributed to the recrystallization of water-insoluble oligosaccharides during the purification process. CNCs extracted from mercerized MCP exhibited the coexistence of two cellulose II populations, while mercerized MFC produced predominantly flake-like nanoparticles.

Beyond conventional rod-like CNCs, room-temperature hydrolysis enabled access to unconventional nanostructures, including hierarchical, surface-decorated CNCs and compact flake-like particles. The hierarchical structures consist of particles decorated with smaller surface features, likely composed of cellulose II crystallites originating from precipitated cello-oligosaccharides, while the flake-like CNCs are interpreted as the result of a distinct fragmentation–reassembly pathway promoted by low crystallinity, mercerization-induced swelling, and suppressed hydrolysis kinetics. Importantly, the emergence of these morphologies reflects a controlled kinetic regime rather than incomplete or unsuccessful hydrolysis.

Overall, the results confirm the initial hypothesis that the interplay between cellulose source, mercerization pretreatment, and hydrolysis conditions dictates the crystalline structure and morphology of CNCs. By suppressing thermal activation, low-temperature acid hydrolysis functions as a structure-directing experimental framework that provides access to non-classical CNC architectures and offers mechanistic insight into cellulose depolymerization, recrystallization, and nanostructure assembly. By enabling the production of CNCs with tailored architecture, surface composition, and associated physicochemical properties, this approach opens new opportunities for the rational design of cellulose-based nanomaterials in advanced applications such as nanocomposites, coatings, and biomedical systems.

CRediT authorship contribution statement

Andrea Riccioni: Writing – original draft, Visualization, Methodology, Investigation, Conceptualization. **Jean-Luc Putaux:** Writing – review & editing, Methodology, Investigation. **Matthieu Fumagalli:** Writing – review & editing, Supervision, Methodology. **Silvia Maria Ronchetti:** Writing – original draft, Investigation. **Sara Ferraris:** Writing – original draft, Investigation. **Roberta Bongiovanni:** Writing – review & editing, Supervision, Resources. **Alessandra Vitale:** Writing – review & editing, Supervision, Funding acquisition.

Declaration of competing interest

The authors declare that they have no known competing financial interests or personal relationships that could have appeared to influence the work reported in this paper.

Acknowledgements

We thank the NanoBio-ICMG platform (UAR 2607, Grenoble) for granting access to the electron microscopy facility, the PCANS chromatography platform at CERMAV for the sugar analysis of the starting materials, and Francesca Demichelis from the Department of Applied Science and Technology of Politecnico di Torino for elemental analysis. Part of this study was carried out within the "Sustainable rubber composite Materials by Dynamic covalent networks And BIO-fillers – MadABio" project – funded by European Union – Next Generation EU within the PRIN 2022 PNRR program (D.D.1409 del 14/09/2022 Ministero dell'Università e della Ricerca).

Supplementary materials

Supplementary material associated with this article can be found, in the online version, at doi:10.1016/j.carpta.2026.101125.

Data availability

Data will be made available on request.

References

Abitbol, T., Kloser, E., & Gray, D. G. (2013). Estimation of the surface sulfur content of cellulose nanocrystals prepared by sulfuric acid hydrolysis. *Cellulose, 20*(2), 785–794. https://doi.org/10.1007/s10570-013-9871-0

Amara, C., El Mahdi, A., Medimagh, R., & Khwaldia, K. (2021). Nanocellulose-based composites for packaging applications. *Current Opinion in Green and Sustainable Chemistry*. https://doi.org/10.1016/j.cogsc.2021.100512, 31.

Babaei-Ghazvini, A., Vafakish, B., Patel, R., Falua, K. J., Dunlop, M. J., & Acharya, B. (2024). Cellulose nanocrystals in the development of biodegradable materials: A review on CNC resources, modification, and their hybridization. *International Journal of Biological Macromolecules, 258*. https://doi.org/10.1016/j.ijbiomac.2023.128834. VolElsevier B.V.

Bahsaine, K., El Allaoui, B., Benzeid, H., El Achaby, M., Zari, N., El Kacem Qaiss, A., & Bouhfid, R. (2023). Hemp cellulose nanocrystals for functional chitosan/polyvinyl alcohol-based films for food packaging applications. *RSC Advances, 13*(47), 33294–33304. https://doi.org/10.1039/d3ra06586c

Bellmann, C., Caspari, A., Moitzi, C., & Babick, F. (2019). *Dynamic and electrphoretic light scattering, Guidlines for particle-size analysis and zeta potential determination*. In (Anton Paar, Ed.).

Bhattacharjee, S. (2016). DLS and zeta potential - what they are and what they are not? *Journal of Controlled Release, 235*, 337–351. https://doi.org/10.1016/j.jconrel.2016.06.017

Bouchard, J., Méthot, M., Fraschini, C., & Beck, S. (2016). Effect of oligosaccharide deposition on the surface of cellulose nanocrystals as a function of acid hydrolysis temperature. *Cellulose, 23*(6), 3555–3567. https://doi.org/10.1007/s10570-016-1036-5

Brito, B. S. L., Pereira, F. V., Putaux, J. L., & Jean, B. (2012). Preparation, morphology and structure of cellulose nanocrystals from bamboo fibers. *Cellulose, 19*(5), 1527–1536. https://doi.org/10.1007/s10570-012-9738-9

Buchert, J., Tenkanen, M., Kantelinen, A., & Viikari, L. (1994). Application of xylanases in the pulp and paper industry. *Bioresource Technology, 50*, 65–72. https://doi.org/10.1016/0960-8524(94)90222-4

Camargos, C. H. M., & Rezende, C. A. (2021). Structure-property relationships of cellulose nanocrystals and nanofibrils: Implications for the design and performance of nanocomposites and all-nanocellulose systems. *ACS Applied Nano Materials, 4*(10), 10505–10518. https://doi.org/10.1021/acsanm.1c02008

Chanthathamrongsiri, N., Petchsomrit, A., Leelakanok, N., Siranonthana, N., & Sirirak, T. (2021). The comparison of the properties of nanocellulose isolated from colonial and solitary marine tunicates. *Heliyon, 7*(8). https://doi.org/10.1016/j.heliyon.2021.e07819

Chen, L., Wang, Q., Hirth, K., Baez, C., Agarwal, U. P., & Zhu, J. Y. (2015). Tailoring the yield and characteristics of wood cellulose nanocrystals (CNC) using concentrated acid hydrolysis. *Cellulose, 22*(3), 1753–1762. https://doi.org/10.1007/s10570-015-0615-1

Dhar, P., Tarafder, D., Kumar, A., & Katiyar, V. (2015). Effect of cellulose nanocrystal polymorphs on mechanical, barrier and thermal properties of poly(lactic acid) based bionanocomposites. *RSC Advances, 5*(74), 60426–60440. https://doi.org/10.1039/c5ra06840a

Ferro, M., Mannu, A., Panzeri, W., Theeuwen, C. H. J., & Mele, A. (2020). An integrated approach to optimizing cellulose mercerization. *Polymers, 12*(7), 1–16. https://doi.org/10.3390/polym12071559

Filson, P. B., & Dawson-Andoh, B. E. (2009). Sono-chemical preparation of cellulose nanocrystals from lignocellulose derived materials. *Bioresource Technology, 100*(7), 2259–2264. https://doi.org/10.1016/J.BIORTECH.2008.09.062

Flauzino Neto, W. P., Putaux, J. L., Mariano, M., Ogawa, Y., Otaguro, H., Pasquini, D., & Dufresne, A. (2016). Comprehensive morphological and structural investigation of cellulose i and II nanocrystals prepared by sulphuric acid hydrolysis. *RSC Advances, 6*(79). https://doi.org/10.1039/c6ra16295a

French, A. D. (2014). Idealized powder diffraction patterns for cellulose polymorphs. *Cellulose, 21*(2), 885–896. https://doi.org/10.1007/s10570-013-0030-4

Gaynor, J. G., Agwuncha, S. C., Smith, A., Gaynor, G., Harrington, M. J., & Lucia, L. (2024). Alkaline pretreatment and soda pulping of genetically improved hemp. *Industrial Crops and Products*, 211. https://doi.org/10.1016/j.indcrop.2024.118181

Gong, J., Li, J., Xu, J., Xiang, Z., & Mo, L. (2017). Research on cellulose nanocrystals produced from cellulose sources with various polymorphs. *RSC Advances, 7*(53), 33486–33493. https://doi.org/10.1039/c7ra06222b

Haafiz, M. K. M., Hassan, A., Zakaria, Z., & Inuwa, I. M. (2014). Isolation and characterization of cellulose nanowhiskers from oil palm biomass microcrystalline

cellulose. *Carbohydrate Polymers, 103*(1), 119–125. https://doi.org/10.1016/j.carbpol.2013.11.055

Habibi, Y., Lucia, L. A., & Rojas, O. J. (2010). Cellulose nanocrystals: Chemistry, self-assembly, and applications. *Chemical Reviews, 110*(6), 3479–3500. https://doi.org/10.1021/cr900339w

Halonen, H., Larsson, P. T., & Iversen, T. (2013). Mercerized cellulose biocomposites: A study of influence of mercerization on cellulose supramolecular structure, water retention value and tensile properties. *Cellulose, 20*(1), 57–65. https://doi.org/10.1007/s10570-012-9801-6

Han, J., Zhou, C., French, A. D., Han, G., & Wu, Q. (2013). Characterization of cellulose II nanoparticles regenerated from 1-butyl-3-methylimidazolium chloride. *Carbohydrate Polymers, 94*(2), 773–781. https://doi.org/10.1016/j.carbpol.2013.02.003

Haouache, S., Jimenez-Saelices, C., Cousin, F., Falourd, X., Pontoire, B., Cahier, K., Jérome, F., & Capron, I. (2022). Cellulose nanocrystals from native and mercerized cotton. *Cellulose, 29*(3), 1567–1581. https://doi.org/10.1007/s10570-021-04313-8

Hattori, T., Ogata, M., Kameshima, Y., Totani, K., Nikaido, M., Nakamura, T., Koshino, H., & Usui, T. (2012). Enzymatic synthesis of cellulose II-like substance via cellulolytic enzyme-mediated transglycosylation in an aqueous medium. *Carbohydrate Research, 353*, 22–26. https://doi.org/10.1016/j.carres.2012.03.018

Hu, T. Q., Hashaikeh, R., & Berry, R. M. (2014). Isolation of a novel, crystalline cellulose material from the spent liquor of cellulose nanocrystals (CNCs). *Cellulose, 21*(5), 3217–3229. https://doi.org/10.1007/s10570-014-0350-z

Hubbe, M. A., Sjöstrand, B., Lestelius, M., Håkansson, H., Swerin, A., & Henriksson, G. (2024). Swelling of cellulosic fibers in aqueous systems: A review of chemical and mechanistic factors. *BioResources, 19*(3). https://doi.org/10.15376/biores.19.3.Hubbe

Jia, C., Chen, L., Shao, Z., Agarwal, U. P., Hu, L., & Zhu, J. Y. (2017). Using a fully recyclable dicarboxylic acid for producing dispersible and thermally stable cellulose nanomaterials from different cellulosic sources. *Cellulose, 24*(6), 2483–2498. https://doi.org/10.1007/s10570-017-1277-y

Kalia, S., Kaith, B. S., & Kaur, I. (2009). Pretreatments of natural fibers and their application as reinforcing material in polymer composites-a review. *Polymer Engineering and Science, 49*(7), 1253–1272. https://doi.org/10.1002/pen.21328

Leong, S. L., Tiong, S. I. X., Siva, S. P., Ahamed, F., Chan, C. H., Lee, C. L., Chew, I. M. L., & Ho, Y. K. (2022). Morphological control of cellulose nanocrystals via sulfuric acid hydrolysis based on sustainability considerations: An overview of the governing factors and potential challenges. *Journal of Environmental Chemical Engineering, 10*(4). https://doi.org/10.1016/j.jece.2022.108145

Li, J., Wang, Z., Wang, P., Tian, J., Liu, T., Guo, J., Zhu, W., Khan, M. R., Xiao, H., & Song, J. (2024). Effects of hydrolysis conditions on the morphology of cellulose II nanocrystals (CNC-II) derived from mercerized microcrystalline cellulose. *International Journal of Biological Macromolecules*, 258. https://doi.org/10.1016/j.ijbiomac.2023.128936

Lin, L., Jiang, T., Liang, Y., Zhu, W., Inamdar, U. Y., Pervez, M. N., Navik, R., Yang, X., Cai, Y., & Naddeo, V. (2022). Combination of pre-and post-mercerization processes for cotton fabric. *Materials, 15*(6). https://doi.org/10.3390/ma15062092

Liu, Y., Wang, H., Yu, G., Yu, Q., Li, B., & Mu, X. (2014). A novel approach for the preparation of nanocrystalline cellulose by using phosphotungstic acid. *Carbohydrate Polymers, 110*, 415–422. https://doi.org/10.1016/j.carbpol.2014.04.040

Luzi, F., Fortunati, E., Puglia, D., Lavorgna, M., Santulli, C., Kenny, J. M., & Torre, L. (2014). Optimized extraction of cellulose nanocrystals from pristine and carded hemp fibres. *Industrial Crops and Products, 56*, 175–186. https://doi.org/10.1016/j.indcrop.2014.03.006

Meurs, E., Antonsson, S., Carlsson Kvarnlöf, G., Henriksson, G., & Håkansson, H. (2026). Comparing swelling and liquid retention of pulps from textile waste and conventional dissolving pulps. *Cellulose, 33*(3), 1239–1254. https://doi.org/10.1007/s10570-026-06943-2

Najafi, Z., & Kahyaoglu, L. N. (2024). Biodegradable active films based on Chlorella biomass and cellulose nanocrystals isolated from hemp stalk fibers. *Food Bioscience, 62*. https://doi.org/10.1016/j.fbio.2024.105142

Niinivaara, E., Vanderfleet, O. M., Kontturi, E., & Cranston, E. D. (2021). Tuning the physicochemical properties of cellulose nanocrystals through an in situ oligosaccharide surface modification method. *Biomacromolecules, 22*(8), 3284–3296. https://doi.org/10.1021/acs.biomac.1c00384

Park, S., Baker, J. O., Himmel, M. E., Parilla, P. A., & Johnson, D. K. (2010). Cellulose crystallinity index: Measurement techniques and their impact on interpreting cellulase performance. *Biotechnology for Biofuels*. https://doi.org/10.1186/1754-6834-3-10

Pawcenis, D., Leśniak, M., Szumera, M., Sitarz, M., & Profic-Paczkowska, J. (2022). Effect of hydrolysis time, pH and surfactant type on stability of hydrochloric acid hydrolyzed nanocellulose. *International Journal of Biological Macromolecules, 222*, 1996–2005. https://doi.org/10.1016/j.ijbiomac.2022.09.289

Pérez, J., Muñoz-Dorado, J., De La Rubia, T., & Martínez, J. (2002). Biodegradation and biological treatments of cellulose, hemicellulose and lignin: An overview. *International Microbiology, 5*(2), 53–63. https://doi.org/10.1007/s10123-002-0062-3

Phanthong, P., Reubroycharoen, P., Hao, X., Xu, G., Abudula, A., & Guan, G. (2018). Nanocellulose: Extraction and application. *Carbon Resources Conversion, 1*(1), 32–43. https://doi.org/10.1016/j.crcon.2018.05.004

Ray, D., & Sarkar, B. K. (2001). Characterization of Alkali-treated jute fibers for physical and mechanical properties. *Journal of Applied Polymer Science, 80*, 1013–1020. https://doi.org/10.1002/app.1184

Reid, M. S., Villalobos, M., & Cranston, E. D. (2017). Benchmarking cellulose nanocrystals: From the laboratory to industrial production. In *Langmuir, 33* pp. 1583–1598). American Chemical Society. https://doi.org/10.1021/acs.langmuir.6b03765. VolNumber.

Revol, J. F., Dietrich, A., & Goring, D. A. I. (1986). Effect of mercerization on the crystallite size and crystallinity index in cellulose from different sources. *Canadian Journal of Chemistry*. https://doi.org/10.1139/v87-288

Salem, K. S., Kasera, N. K., Rahman, M. A., Jameel, H., Habibi, Y., Eichhorn, S. J., French, A. D., Pal, L., & Lucia, L. A. (2023). Comparison and assessment of methods for cellulose crystallinity determination. *Chemical Society Reviews, 52*(18), 6417–6446. https://doi.org/10.1039/d2cs00569g

Sarı, B., & Kaynak, C. (2025). Obtaining cellulose nanocrystals by acid hydrolysis procedure; and their use as reinforcement in polylactide biocomposites. *Journal of Thermoplastic Composite Materials, 38*(3), 1040–1062. https://doi.org/10.1177/08927057241254101

O'sullivan, A. C. (1997). Cellulose: The structure slowly unravels. *Cellulose, 4*, 173–207. https://doi.org/10.1023/A:1018431705579

Scherrer, P. (1918). Bestimmung der Grösse und der inneren von Kolloidteilchen mittels Röntgenstrahlen Struktur Nachr. Nachrichten von der Gesellschaft der Wissenschaften zu Göttingen. Mathematisch-physikalische Klasse, 98–100.

Sèbe, G., Ham-Pichavant, F., Ibarboure, E., Koffi, A. L. C., & Tingaut, P. (2012). Supramolecular structure characterization of cellulose II nanowhiskers produced by acid hydrolysis of cellulose i substrates. *Biomacromolecules, 13*(2), 570–578. https://doi.org/10.1021/bm201777j

Seddiqi, H., Oliaei, E., Honarkar, H., Jin, J., Geonzon, L. C., Bacabac, R. G., & Klein-Nulend, J. (2021). Cellulose and its derivatives: Towards biomedical applications. *Cellulose, 28*(4), 1893–1931. https://doi.org/10.1007/s10570-020-03674-w

Segal, L., Creely, J. J., Martin, A. E., & Conrad, C. M. (1959). An empirical method for estimating the degree of crystallinity of native cellulose using the X-ray diffractometer. *Textile Research Journal, 43*, 786–794. https://doi.org/10.1177/004051755902901003

Sharma, S., Nair, S. S., Zhang, Z., Ragauskas, A. J., & Deng, Y. (2015). Characterization of micro fibrillation process of cellulose and mercerized cellulose pulp. *RSC Advances, 5*(77), 63111–63122. https://doi.org/10.1039/c5ra09068g

Shibazaki, H., Kuga, S., & Okano, T. (1997). Mercerization and acid hydrolysis of bacterial cellulose. *Cellulose, 4*, 75–87. https://doi.org/10.1023/A:1024273218783

Shojaeiarani, J., Bajwa, D. S., & Chanda, S. (2021). Cellulose nanocrystal based composites: A review. *Composites Part C: Open Access, 5*. https://doi.org/10.1016/j.jcomc.2021.100164

Song, K., Zhu, X., Zhu, W., & Li, X. (2019). Preparation and characterization of cellulose nanocrystal extracted from Calotropis procera biomass. *Bioresources and Bioprocessing, 6*(1). https://doi.org/10.1186/s40643-019-0279-z

Tang, Y., Yang, H., & Vignolini, S. (2022). Recent progress in production methods for cellulose nanocrystals: Leading to more sustainable processes. In *Advanced sustainable systems, 6*. John Wiley and Sons Inc. https://doi.org/10.1002/adsu.202100100. VolNumber 3.

Tarrés, Q., Aguado, R., Zoppe, J. O., Mutjé, P., Fiol, N., & Delgado-Aguilar, M. (2022). Dynamic light scattering plus scanning electron microscopy: Usefulness and limitations of a simplified estimation of nanocellulose dimensions. *Nanomaterials, 12*(23). https://doi.org/10.3390/nano12234288

Taylor, J. B. (1957). The water solubilities and heats of solutions of short chain cellulose oligosaccharides. *Transactions of the Faraday Society*, 1198–1203. https://doi.org/10.1039/TF9575301198

Thomas, B., Raj, M. C., Athira, B. K., Rubiyah, H. M., Joy, J., Moores, A., Drisko, G. L., & Sanchez, C. (2018). Nanocellulose, a versatile green platform: From biosources to materials and their applications. *Chemical Reviews,, 118*(24), 11575–11625. https://doi.org/10.1021/acs.chemrev.7b00627

Wang, Q. Q., Zhu, J. Y., Reiner, R. S., Verrill, S. P., Baxa, U., & McNeil, S. E. (2012). Approaching zero cellulose loss in cellulose nanocrystal (CNC) production: Recovery and characterization of cellulosic solid residues (CSR) and CNC. *Cellulose, 19*(6), 2033–2047. https://doi.org/10.1007/s10570-012-9765-6

Xing, L., Gu, J., Zhang, W., Tu, D., & Hu, C. (2018). Cellulose I and II nanocrystals produced by sulfuric acid hydrolysis of Tetra pak cellulose I. *Carbohydrate Polymers, 192*, 184–192. https://doi.org/10.1016/j.carbpol.2018.03.042

Yu, X., Jiang, Y., Wu, Q., Wei, Z., Lin, X., & Chen, Y. (2021). Preparation and characterization of cellulose nanocrystal extraction from pennisetum hydridum fertilized by municipal sewage sludge via sulfuric acid hydrolysis. *Frontiers in Energy Research, 9*. https://doi.org/10.3389/fenrg.2021.774783

Yue, Y., Han, G., & Wu, Q. (2013). Cotton fiber transitional properties. *BioResources, 8*(4), 6460–6471. https://doi.org/10.15376/biores.8.4.6460-6471

Zhao, Y., & Li, J. (2014). Excellent chemical and material cellulose from tunicates: Diversity in cellulose production yield and chemical and morphological structures from different tunicate species. *Cellulose, 21*(5), 3427–3441. https://doi.org/10.1007/S10570-014-0348-6

Zhu, W., & Theliander, H. (2015). Precipitation of lignin from softwood black liquor: An investigation of the equilibrium and molecular properties of lignin. *BioResources, 10*(1), 1696–1714. https://doi.org/10.15376/biores.10.1.1696-1715

Zuluaga, R., Putaux, J. L., Cruz, J., Vélez, J., Mondragon, I., & Gañán, P. (2009). Cellulose microfibrils from banana rachis: Effect of alkaline treatments on structural and morphological features. *Carbohydrate Polymers, 76*(1), 51–59. https://doi.org/10.1016/j.carbpol.2008.09.024